The Astrophysical Journal, 743:57 (11pp), 2011 December 10 doi:10.1088/0004-637X/743/1/57

ONE-DIMENSIONAL MODELING FOR TEMPERATURE-DEPENDENT UPFLOW IN THE DIMMING REGION OBSERVED BY *HINODE*/EUV IMAGING SPECTROMETER

S. Imada[1], H. Hara[2], T. Watanabe[2], I. Murakami[3], L. K. Harra[4], T. Shimizu[1], and E. G. Zweibel[5]
[1] Institute of Space and Astronautical Science, Japan Aerospace Exploration Agency, 3-1-1 Yoshinodai, Chuo-ku, Sagamihara-shi, Kanagawa 252-5210, Japan
[2] National Astronomical Observatory of Japan, 2-21-1 Osawa, Mitaka-shi, Tokyo 181-8588, Japan
[3] National Institute for Fusion Science, 322-6 Oroshi-cho, Toki, Gifu 509-5292, Japan
[4] UCL-Mullard Space Science Laboratory, Holmbury St Mary, Dorking, Surrey, RH5 6NT, UK
[5] Department of Astronomy, University of Wisconsin-Madison, 475 N Charter Street, Madison, WI 53706, USA
Received 2011 July 22; accepted 2011 August 24; published 2011 November 22

ABSTRACT

We previously found a temperature-dependent upflow in the dimming region following a coronal mass ejection observed by the *Hinode* EUV Imaging Spectrometer (EIS). In this paper, we reanalyzed the observations along with previous work on this event and provided boundary conditions for modeling. We found that the intensity in the dimming region dramatically drops within 30 minutes from the flare onset, and the dimming region reaches the equilibrium stage after ∼1 hr. The temperature-dependent upflows were observed during the equilibrium stage by EIS. The cross-sectional area of the flux tube in the dimming region does not appear to expand significantly. From the observational constraints, we reconstructed the temperature-dependent upflow by using a new method that considers the mass and momentum conservation law and demonstrated the height variation of plasma conditions in the dimming region. We found that a super-radial expansion of the cross-sectional area is required to satisfy the mass conservation and momentum equations. There is a steep temperature and velocity gradient of around 7 Mm from the solar surface. This result may suggest that the strong heating occurred above 7 Mm from the solar surface in the dimming region. We also showed that the ionization equilibrium assumption in the dimming region is violated, especially in the higher temperature range.

Key words: magnetohydrodynamics (MHD) – plasmas – Sun: corona – Sun: flares – Sun: UV radiation

Online-only material: color figures

1. INTRODUCTION

A solar flare is often explained as a rapid energy conversion phenomenon from magnetic field energy to plasma energy. The energy released by a flare is so huge that the total amount of energy often reaches 10^{32} erg within an hour. Over the past few decades, considerable effort has been devoted toward understanding the physical mechanism of solar flares, and various models have been proposed (e.g., Carmichael 1964; Sturrock 1966; Hirayama 1974; Kopp & Pneuman 1976). Nowadays, it is widely accepted that magnetic reconnection is regarded as the fundamental energy conversion mechanism of eruptive flares. So far, various features expected from the model have been discussed and confirmed by observations (e.g., Tsuneta et al. 1992; Ohyama & Shibata 1998; Yokoyama et al. 2001; Teriaca et al. 2003).

Another important aspect of the solar flare is its impact on its surroundings. The most powerful flares are associated with a coronal mass ejection (CME; e.g., Kahler 1992; Yashiro et al. 2006). Because a CME releases a huge amount of plasma and magnetic field into the interplanetary space in a short duration of time, the equilibrium in the solar corona breaks down. Therefore, a large-scale magnetic reconfiguration in the solar corona occurs. The opposite scenario can also work; a large-scale magnetic reconfiguration can cause a CME. Although the causal relationship between large-scale magnetic reconfigurations and CMEs is still not clear, a solar flare has a large impact on its surroundings through a CME or large-scale magnetic reconfiguration.

Coronal dimming in the EUV and/or soft-X-ray range (e.g., Rust 1983; Sterling & Hudson 1997; Thompson et al. 1998), which is due to a loss of coronal plasma, is often observed as one of the main on-disk signatures of a CME. The dimming can persist longer than a day in some extreme cases, and its mass loss contribution can reach more than 50% of the total mass of the CME (e.g., Sterling & Hudson 1997). There are two scenarios that can explain the origin of dimming regions. One is the eruption of a flux rope, and the other is interchange reconnection between closed and open magnetic field lines. Sterling & Hudson (1997) found a pair of dimming regions which are located at either end of a pre-flare sigmoidal (S-shaped) structure. They concluded that their findings are consistent with the source of the CME being a flux rope that erupted, leaving behind the dimming regions. Attrill et al. (2006) discussed the magnetic field topology change associated with a CME. In this scenario, the magnetic loops of the CME expand and eventually push against the oppositely oriented open magnetic field of the polar coronal hole. This triggers a successive magnetic reconnection, and some part of the magnetic loop topology changes from closed to open. Although it is not clear which is the dominant process, in either case the dimming region is likely to be a footpoint of an open field line. The changing magnetic configuration from closed to open within a short period causes the evacuation of coronal material toward interplanetary space through the rarefaction wave, and plasma cannot refill the open magnetic field lines for a long time.

Quantitative measurements of dimming regions are essential to understand its contribution to CME formation or development. The EUV Imaging Spectrometer (EIS) on board *Hinode* (Kosugi et al. 2007) provides EUV spectra with higher spectral and spatial resolution than ever before (Culhane et al. 2007). The first measurement of dimming regions by EIS was the flares and CMEs of 2006 December 13 and 14 in NOAA 10930. Harra et al. (2007) studied the outflows in the dimming region of the

2006 December 14 events, and they found for the first time that the strong outflow exists at the loop footpoints in the dimming region that is located far away from the flare site. Imada et al. (2007) analyzed the flare of 2006 December 13 and found a temperature dependence of the outflows; the hotter plasma shows the faster upflow. They claimed that the temperature-dependent upflows are the consequence of coupling between heating and bulk acceleration along the line-of-sight (height direction). Jin et al. (2009) have analyzed both of these 2006 December events and found that the velocity also correlates with the photospheric magnetic field. Harra et al. (2011) discussed the magnetic flux from the source of the CME by using the Doppler velocity difference and the photospheric magnetic field measurement. They found that their estimation was consistent with the magnetic flux in the magnetic cloud observed at the interplanetary medium (1 AU) by in situ measurement.

In this paper, we explore further the temperature-dependent upflow in the dimming region observed by *Hinode*/EIS. The aim of our paper is to reconstruct the temperature-dependent upflow by using a new method that uses the mass and momentum conservation law to determine the height variation of the plasma conditions in the dimming region. This paper is organized as follows. In the next section, we discuss the observational properties in the dimming region of the 2006 December 13 event. Section 3 is devoted to the modeling of temperature-dependent upflow. We discuss the time-dependent ionization effect in Section 4. The summary and discussion are given in Section 5.

2. OBSERVATION OF THE DIMMING REGION

In this section, we discuss the observational properties in the dimming region on the 2006 December 13 event. We have reanalyzed the event to obtain quantitative information to reconstruct the dimming region, which is discussed in the next section. We also discuss the previous observational results of the same event.

2.1. Instrumentation

The EIS instrument on board *Hinode* is a high spectral resolution spectrometer aimed at studying dynamic phenomena in the corona with high spatial resolution and sensitivity. While making a large raster scan with 1 arcsec slit from 01:12 UT to 05:42 UT on 2006 December 13, EIS observed an X3.2 flare. The flare occurred at 02:14 UT accompanied by the halo CME. The flare itself has been studied in detail (e.g., Kubo et al. 2007; Imada et al. 2008; Asai et al. 2008; Minoshima et al. 2009). EIS data from the raster were processed using the software provided by the EIS team (EIS_PREP), which corrects for the flat field, dark current, cosmic rays, and hot pixels. Each spectrum was fitted with a Gaussian profile, and the line width and Doppler velocity were determined. The slit tilt was corrected by eis_tilt_correction. For thermal reasons, there is an orbital variation of the line position causing an artificial Doppler shift of $+/-$ 20 km s^{-1}, which follows a sinusoidal behavior. This orbital variation of the line position was corrected using the method described by Imada et al. (2007), and the instrumental effects are reduced to below $+/-$ 5 km s^{-1} as a result.

To study the time evolution of the dimming region, we made use of the Extreme ultraviolet Imaging Telescope (EIT) on *Solar and Heliospheric Observatory* (*SOHO*; Delaboundiniére et al. 1995). We used the EIT images in the 195 Å filter. The EIT data have a cadence of 12 minutes and a pixel size of 2.6 arcsec pixels. The exposure times are ∼12.6 s during the event. We processed EIT data by using eit_prep for the calibration.

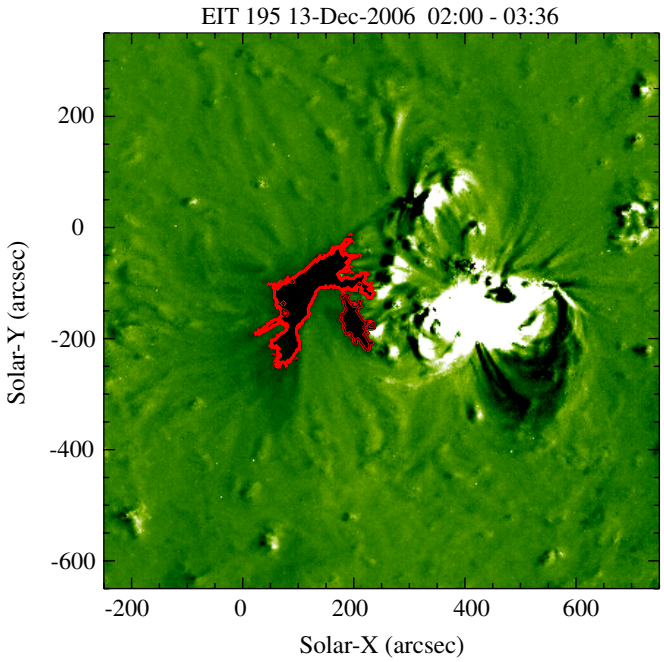

Figure 1. EIT base difference image with pre-flare image at December 13, 02:00 UT subtracted from the image on December 13, 03:36 UT. The red contour represents the dimming region.

(A color version of this figure is available in the online journal.)

2.2. SOHO/EIT Observation

An EIT base difference image using the 195 Å filter is shown in Figure 1. A pre-flare image at 02:00 UT was subtracted from the post-flare image at 03:36 UT. The flare site is located around (350, −150), and there is a deep dark dimming region in the far east from the flare site. We highlighted the dimming region in which the intensity drops by more than 60% of its original intensity with a red contour. The time evolution of the dimming region can be clearly seen in Figure 2. Most loops or diffuse structures inside the red contour were blown off within the first 30 minutes, and the bright point-like structures, which may be related to foot points of coronal loops, lose their intensity gradually. Figure 3 shows the time evolution of the average intensity in the dimming region (inside the red contour in Figure 1). We can clearly see that the intensity is rapidly decreasing and reaching the quasi-equilibrium stage. Similar features were observed in the event of the next day (e.g., Harra et al. 2007). Long-term evolution of this dimming region is discussed by Attrill et al. (2010). They found that concentrated downflows develop during the recovery phase of the dimmings and are also correlated with the same magnetic elements that were related to outflows during the quasi-equilibrium stage.

2.3. Hinode/EIS Observation

EIS observed the dimming region from 04:00 to 05:30 UT and obtained the spectral information in several emission lines. During this period, the dimming region had already reached the quasi-equilibrium stage (see Figure 3). In Figure 4, we show the intensity, velocity, and line width map of He II (256.32 Å; $\log T_{\max} = 4.70$), Fe XII (195.12 Å; $\log T_{\max} = 6.11$), and Fe XV

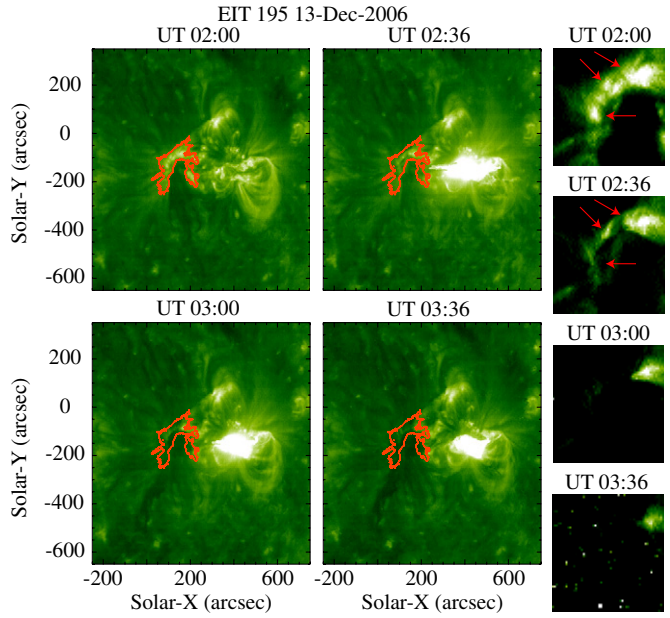

Figure 2. Time series of the dimming region. The right figures are the magnified figures of the dimming region. The red arrows show the bright region inside the dimming region. The color scale was changed from the left figures.

(A color version of this figure is available in the online journal.)

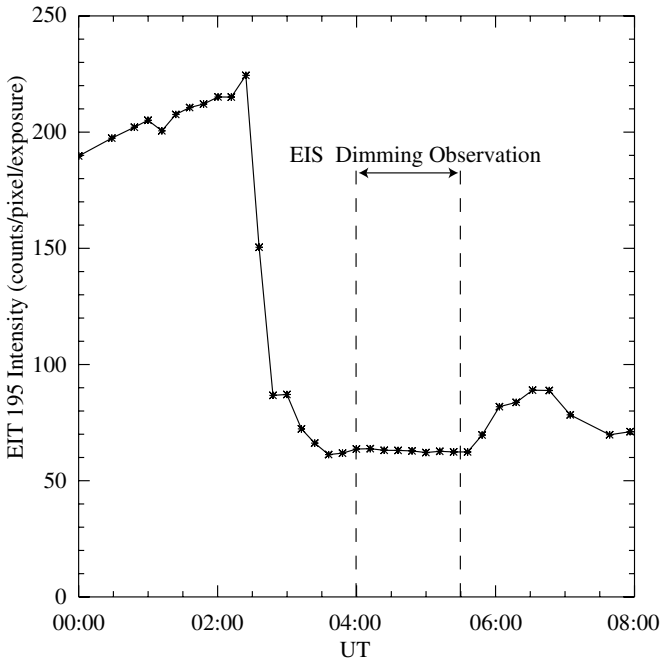

Figure 3. Time variation of the intensity in the dimming region (inside the red contour in Figure 1). The EIS observing time of the dimming region is also shown.

(284.16 Å; $\log T_{\max} = 6.30$) obtained by EIS. The color scales in the velocity map range from −150 to 150 km s^{-1}. The color scales in the line width (full width at half-maximum) map are normalized by the median line width of the whole field of view. The median values of the line widths in He II, Fe XII, and Fe XV are 0.102, 0.073, and 0.085 Å, respectively. Note that EIS scans from west (right) to east (left). The time stamps of slit scanning are also shown in the top of Figure 4. In the intensity map, the bright flare site can be observed in the western part, and we can clearly see the dimming region in the far east from the flare site, which is framed by white dashed lines. The temperature-dependent upflow in the dimming region, which was discussed in Imada et al. (2007) and Jin et al. (2009), was also clearly seen in the Doppler velocity map in Figure 4. The strong outflows (∼100 km s^{-1}) in higher temperature are located in the boundary of the dimming region. The line width in the dimming region also shows the temperature dependence. This is because the inhomogeneities of flows in the dimming region produce spatial variations of Doppler velocities, which result in an apparent broadening of the integrated profile. Therefore, it is reasonable that the line widths in the dimming region also have temperature dependence. The relationship between flows and line broadening is discussed in Imada et al. (2008) and Dolla & Zhukov (2011).

To be confident of our results we need to understand any possible contamination from line blends. Generally, Fe XII and Fe XV lines are very strong in the corona, and we do not need to take into consideration line blending. On the other hand, in the He II line, there are strong line blends with the Si X, which has a formation temperature of $\sim 10^{6.2}$ K (Young et al. 2007). However, the blend is not significant in the dimming region, because the line intensity from the coronal temperature plasma is very weak (Figure 4). Hence, we can neglect the line blend for He II in the dimming region. The line blend in the He II line is also discussed in Jin et al. (2009), and they also concluded that the contribution of the Si X line is more significant in the active regions than in the dimming areas.

In the regions where the Doppler velocity is the highest in Fe XV, we fit the line profiles using a double Gaussian for several ions. The line profiles are clearly separated into two components—the fast upflow and the stationary component (not shown here, see Imada et al. 2007). The fast upflow may correspond to the magnetic field whose topology has been changed from closed to open by the flare activity. The other stationary component may correspond to the magnetic field whose topology was not changed by the flare activity. It is plausible that these two components are mixed within our spatial resolution, because the dimming region locates very far from the flare site. Figure 5 shows the relationship between the velocity (fast) and temperature in the dimming region. The line formation temperatures are defined by the temperature that yields its peak abundance with the CHIANTI code (Landi et al. 2006). This naturally means that we assumed the ionization equilibrium to derive the line formation temperature. The line blending effect does not have a significant effect on the velocity estimation in the result (see Imada et al. 2007). The result of the relationship between the temperature and upflow velocity is also discussed in Jin et al. (2009). The velocities in our result are much faster than those in Jin et al. (2009), because we fitted the line profiles by the double Gaussian. To discuss the relationship between the temperature and velocity quantitatively, we fit it by the following equation:

$$T(v) = a_2 v^2 + a_1 v + a_0, \quad (1)$$

where T, v, and a_{2-0} are the electron temperature (K), upflow velocity (m s^{-1}), and fit coefficients, respectively. The solid line in Figure 5 shows the fitting result, and the fit coefficients are also shown in Table 1. The correlation coefficient (r) is 0.95.

The area of the EIS dimming region at different temperatures in the corona was also studied by Jin et al. (2009). They estimated the area with an intensity drop larger than 5% at the eruption phase compared with the pre-eruption phase. They found

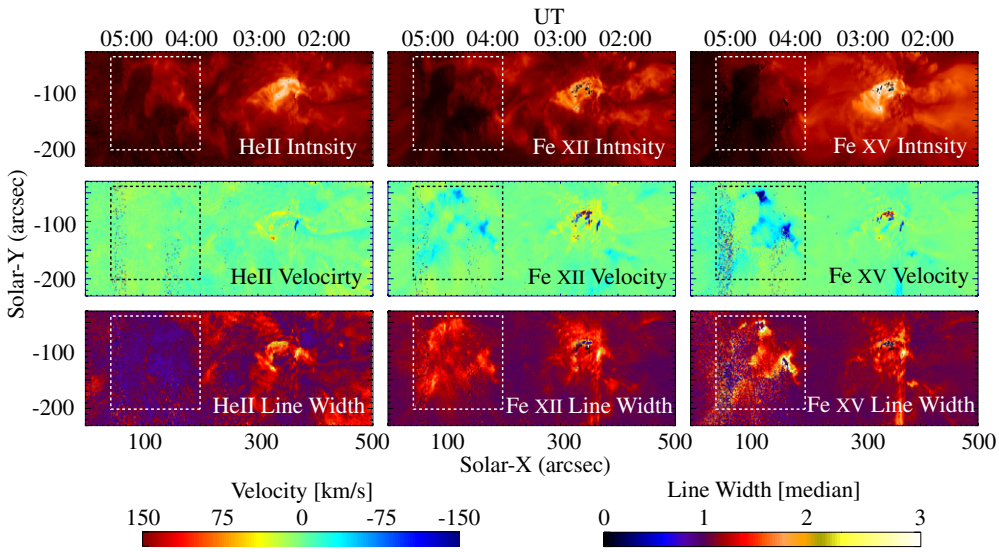

Figure 4. Intensity, velocity, and line width map of the dimming region observed by *Hinode*/EIS. The color scales in the velocity map range from −150 to 150 km s^{-1}. The color scales in the line width (full width at half-maximum) map are normalized by the median line width in the whole field of view. The median line widths of He II, Fe XII, and Fe XV are 0.102, 0.073, and 0.085 Å, respectively.

(A color version of this figure is available in the online journal.)

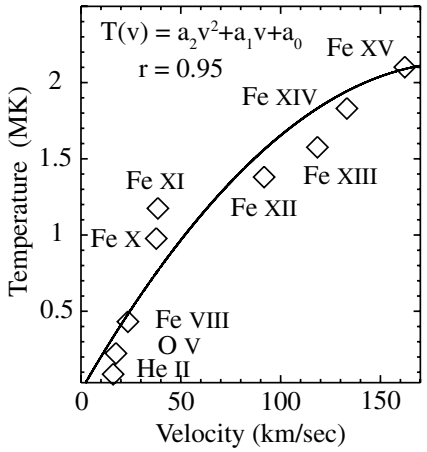

Figure 5. Relationship between temperature and velocity in the dimming region. The velocities were estimated by Doppler velocities, and the line formation temperatures were derived from the ionization equilibrium assumption.

that the dimming area weakly depends on its temperature. From their result, the area increases by a factor of 1.6 between 0.4 and 1.6 MK plasma. They also discussed the relationship between magnetic field and upflow and found that the fast upflows are located at relatively strong magnetic fields.

There are two interpretations for the temperature-dependent upflow in the dimming region. One is that the temperature and velocity depend on the height from the solar surface (line-of-sight direction). The other is that the different loops in the dimming region have different temperatures and velocities in sub-resolution size (the multi-strand model). Both scenarios can explain the temperature-dependent upflows in the dimming region. Recent observations also support both interpretations (e.g., Jin et al. 2009; Robbrecht & Wang 2010; Warren et al. 2011). However, the multi-strand model generally causes large broadening, distortion, and humps in line profile (e.g., Ugarte-Urra & Warren 2011). Therefore, the line profile may not separate into two distinct components (fast and stationary), which is observed by EIS in the dimming region. Further, the

Table 1
Fitting Results

a_2 (K s^2 m^{-2})	a_1 (K s m^{-1})	a_0 (K)
-6.00×10^{-5}	2.27×10^{1}	-2.05×10^{4}

area of the dimming region also weakly depends on the temperature. The observations might support the former scenario, because generally the flux tube expands radially in the solar corona. For those two reasons, we assume that the temperature and velocity depend on the height from the solar surface in the dimming region, although we do not deny the possibility of the multi-strand model.

2.4. Summary of the Observations

A summary of the observations is given below.

1. The intensity (Fe XII) in the dimming region dramatically drops within 30 minutes of the flare onset.
2. The dimming region reaches the equilibrium stage ∼1 hr after the flare onset.
3. EIS observes the temperature-dependent upflows in the dimming region.
4. The dimming region is in the equilibrium stage during the EIS observation period.
5. The temperature dependence of the upflow is characterized by Equation (1).
6. The area of the dimming region weakly depends on the temperature (the expansion factor is ∼1.6 between 0.4 and 1.6 MK plasma).

3. MODELING

3.1. Method for Modeling

In this section, we try to reconstruct the temperature-dependent upflow and determine the height dependence of plasma conditions in the dimming region by using the observational facts discussed in the previous section. Because the

reconstruction will be based on our observations, our model can only apply in the range of 16 km s^{-1} $< v <$ 160 km s^{-1} (0.4MK $< T_e <$ 2 MK). We assumed that the temperature-dependent upflow is quasi-steady, because the flow was observed in the equilibrium stage of the dimming region. The flux tube is vertical to the solar surface, and the cross-sectional area is expanding with height from the solar surface. The flux tube contains low β plasma, and we assumed that cross-field motions are negligible so that a one-dimensional description was adequate. Neglecting time derivatives in the hydrodynamic equations produces the quasi-steady flow model. The mass conservation equation, the equation of the state of fully ionized gas, and the momentum conservation equation in one fluid description are given by

$$mnvA = \text{const}, \tag{2}$$

$$p = 2nk_BT, \tag{3}$$

$$v\frac{dv}{ds} = -\frac{1}{mn}\frac{dp}{ds} - g_0\left(\frac{R_s}{s+R_s}\right)^2, \tag{4}$$

where n, v, A, p, and T are the electron number density, bulk velocity, cross-sectional area, total pressure, and temperature, respectively, m is the mean mass for solar abundances (1.257 times of the hydrogen mass), k_B is the Boltzmann constant, g_0 is the solar surface gravity, R_s is the sun radius, and s is the height from the solar surface. We neglected the effect of He or the other minor elements in Equation (3).

In order to describe the flow precisely, we rewrite Equation (4) using Equations (2) and (3) as follows:

$$\left(v - \frac{2k_BT}{mv}\right)\frac{dv}{ds} + \frac{2k_B}{m}\frac{dT}{ds} = -g_0\left(\frac{R_s}{s+R_s}\right)^2 + \frac{2k_BT}{m}\frac{1}{A}\frac{dA}{ds}. \tag{5}$$

The equation is almost the same as that used for the discussion of the solar wind (Parker 1958) or the discussion of the stationary siphon flows in coronal loops (e.g., Craig & McClymont 1986; Orlando et al. 1995). In a Parker-type wind, the flow is accelerated by a pressure gradient. The pressure drop is typically due to decreases in both temperature and density. In the flow described here, T is increasing with v (see Figure 5). Therefore, we anticipate that acceleration requires rapid divergence of the flux tube area and that the flow is strongly heated.

Equation (5) has a critical point at $v = [2k_BT/m]^{1/2}$. Fortunately, the upflow velocity in the dimming region is less than $[2k_BT/m]^{1/2}$, for example, $[2k_BT/m]^{1/2} = 113$ km s^{-1} at 1 MK. We substitute $T(v)$ (Equation (1)) into Equation (5) and rewrite it in the conservative form as follows:

$$\frac{1}{2}\left(v^2 - v_0^2\right) - \frac{2k_B}{m}\left(\frac{1}{2}a_2\left(v^2 - v_0^2\right) + a_1\left(v - v_0\right) + a_0\log\frac{v}{v_0}\right) + \frac{2k_B}{m}\left(T - T_0\right) = -g_0R_s^2\left(-\frac{1}{s+R_s} + \frac{1}{s_0+R_s}\right) + \frac{2k_B}{m}\int_{s_0}^{s} T\frac{1}{A}\frac{dA}{ds'}ds', \tag{6}$$

where v_0, T_0, and s_0 are the velocity, temperature, and height, respectively, at the base of the coronal loop. We have chosen the footpoint velocity and height to be 16 km s^{-1} and 2000 km, respectively. T_0 can be determined by Equation (1). We simplify each term in Equation (6) as follows: $S_{L1} - S_{L2} + S_{L3} = -S_{R1} + S_{R2}$. The left-hand side in Equation (6) ($S_{L1} - S_{L2} + S_{L3}$) can be determined when the velocity is determined, and the first term of the right-hand side can be determined when the height from the solar surface is determined. Only the second term of the right-hand side (S_{R2}) is unknown. Therefore, we need to assume the cross-sectional area (A) to evaluate Equation (6).

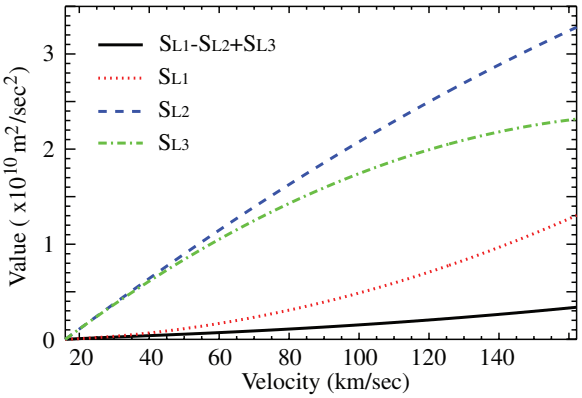

Figure 6. Each term in the left-hand side as a function of velocity in Equation (6). Solid, dotted, dashed, and dash-dotted lines show $S_{L1} - S_{L2} + S_{L3}$, S_{L1}, S_{L2}, and S_{L3}, respectively.

(A color version of this figure is available in the online journal.)

3.2. Radial Expansion of the Flux Tube

The geometry of coronal flux tubes is believed to fan out from the network boundaries in the photosphere to the corona, forming a canopy-like structure (Gabriel 1976). This geometry leads to a varying cross-sectional area of every flux tube along the height of the solar surface. We assumed that the cross-sectional area expands radially, and it can be written as follows:

$$A(s) = A_0\left(\frac{s+R_s}{s_0+R_s}\right)^{\mu}, \tag{7}$$

where μ is the parameter for expansion. The uniform, sub-radial expansion, radial expansion, and super-radial expansion in the cross section can be expressed by $\mu = 0$, $0 < \mu < 2$, $\mu = 2$, and $2 < \mu$, respectively. In all these cases, S_{R2} can be written as follows:

$$S_{R2} = \frac{2k_B\mu}{m}\int_{s_0}^{s} T\frac{1}{s'+R_s}ds'. \tag{8}$$

Furthermore, we can evaluate the integration part in S_{R2} with

$$T_{\rm MAX}\int_{s_0}^{s}\frac{1}{s'+R_s}ds' > \int_{s_0}^{s}T(s')\frac{1}{s'+R_s}ds' > T_0\int_{s_0}^{s}\frac{1}{s'+R_s}ds', \tag{9}$$

where $T_{\rm MAX}$ is the maximum temperature in our range.

The value of each term in the left-hand side of Equation (6) is shown as a function of velocity in Figure 6. We can clearly see that the total of the left-hand side terms always has positive values. In Figure 7, we show S_{R1} as a function of height by the solid line. Note that the horizontal axis in Figures 6 and 7 is different. Let us evaluate S_{R2} in the case of radial expansion ($\mu = 2$). The maximum and minimum values obtained from Equation (9) are shown in Figure 7 by the dashed and dotted lines. Thus, S_{R2} should be located between the dashed and dotted lines. This result indicates that the right-hand side ($-S_{R1}+S_{R2}$) is always negative. Therefore, there is no solution of Equation (6) in the case of radial expansion, because the left-hand side of Equation (6) is always positive.

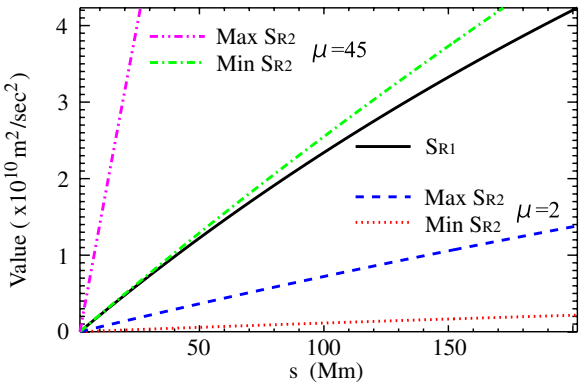

Figure 7. Each term in the right-hand side as a function of height from the solar surface in Equation (6).

(A color version of this figure is available in the online journal.)

3.2.1. Super-radial Expansion: Case I ($\mu = 45$)

From the slope of S_{R1} and S_{R2} at $s = s_0$, we can estimate the lower limit of μ from the positive value in the right-hand side of Equation (6) ($dS_{R2}/ds \geqslant dS_{R1}/ds$):

$$\mu \geqslant \frac{m}{2k_B T_0} \frac{g_0 R_s^2}{s_0 + R_s} \sim 44. \tag{10}$$

Thus, we assumed the super-radial expansion ($\mu = 45$) for the cross-sectional area (Case I). The dot-dashed and double-dot-dashed lines in Figure 7 show the maximum and minimum value of S_{R2} ($\mu = 45$) evaluating from Equation (9). This result indicates that the right-hand side is always positive. Therefore, we can solve Equation (6) with $\mu = 45$ and obtain the height dependence of plasma conditions in the dimming region. We numerically perform the integration of S_{R2}.

The results for the height dependences of various quantities in the dimming region are shown in Figure 8. The horizontal axis shows the height from the solar surface, and the vertical axes show the velocity, temperature, cross-sectional area, and density. The cross-sectional area and density are normalized by those at $s = 2000$ Mm ($=s_0$). The upflow is almost constant until a height of 6 Mm and dramatically accelerates up to 160 km s^{-1} from 6 to 9 Mm. The temperature also shows the same profile as the velocity because of Equation (1). The cross-sectional area expands almost proportionally to the height from the solar surface, and it reaches around 1.6 at 9 Mm. The density is gradually decreasing with the height and rapidly decreasing from 6 Mm. The density ratios (n/n_0) at 7.5 and 9 Mm are almost 0.14 and 0.07, respectively. Note that the temperatures at 7.5 and 9 Mm are around 1.4 and 2 MK, respectively.

3.3. Empirical Model for the Flux Tube

The empirical modeling of the relative size of the flux tube cross-sectional area in the quiet Sun was done by Chae et al. (1998). They obtained the relationship between temperature and velocity from *SOHO*/SUMER observations in the quiet Sun, and derive the estimation of the relative size of the flux tube as a function of temperature. They also found that the derived relative size of the flux tube can be fitted to a functional form suggested by Dowdy et al. (1987) and Rabin (1991):

$$A(T) = A(T_h) \frac{1}{\Gamma} \left(1 + \left(\Gamma^2 - 1\right) \left(\frac{T}{T_h}\right)^{\nu}\right)^{\frac{1}{2}}, \tag{11}$$

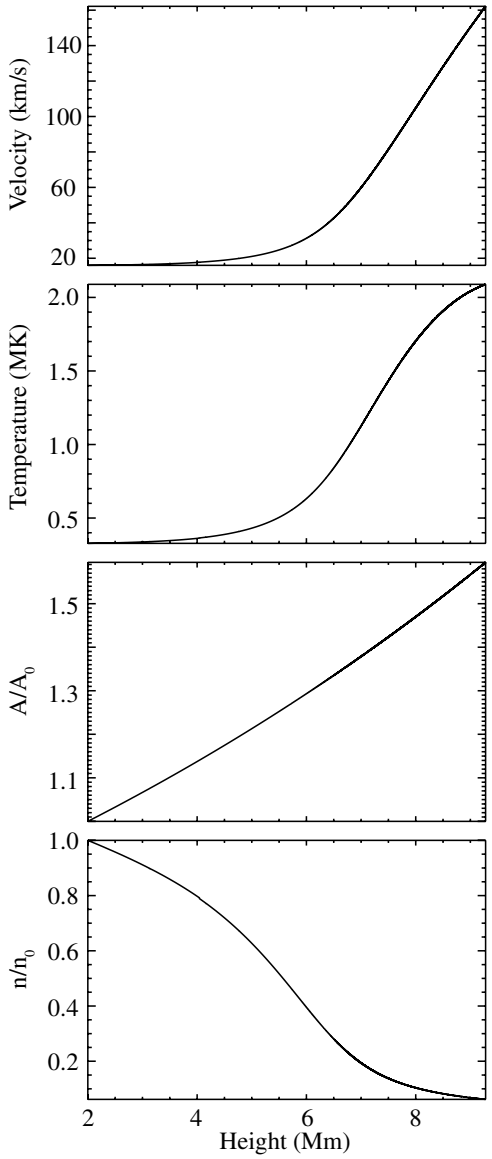

Figure 8. Height variation of plasma conditions in the case of $\mu = 45$ (Case I: super-radial expansion). From top to bottom, velocity, temperature, increase of cross section, and density drop are shown. The cross-sectional area and density are normalized by that at $s = s_0$.

with the values of $T_h = 10^6$ K, $\Gamma = 31$, and $\nu = 3.6$. We applied Equation (11) into Equation (6), and S_{R2} can be written as follows:

$$S_{R2} = \frac{k_B}{m} \frac{\Gamma^2 - 1}{T_h^{\nu}} \int_{T_0}^{T} T'^{\nu} \left(1 + (\Gamma^2 - 1) \left(\frac{T'}{T_h}\right)^{\nu}\right)^{-1} dT'. \tag{12}$$

Their discussion concentrated on the down flows ($\lesssim$10 km s^{-1}) observed in the quiet-Sun transition region (below 1 MK). Although their situation may be different from the dimming region, their results might include the characteristics of the cross-sectional area.

3.3.1. Strong Dependence on Temperature: Case II ($\nu = 3.6$)

First, we have applied the parameters suggested by Chae et al. (1998) ($T_h = 10^6$ K, $\Gamma = 31$, and $\nu = 3.6$) to Equation (12) and solved Equation (6). The results of height dependence in the dimming region are shown in Figure 9. The figure format

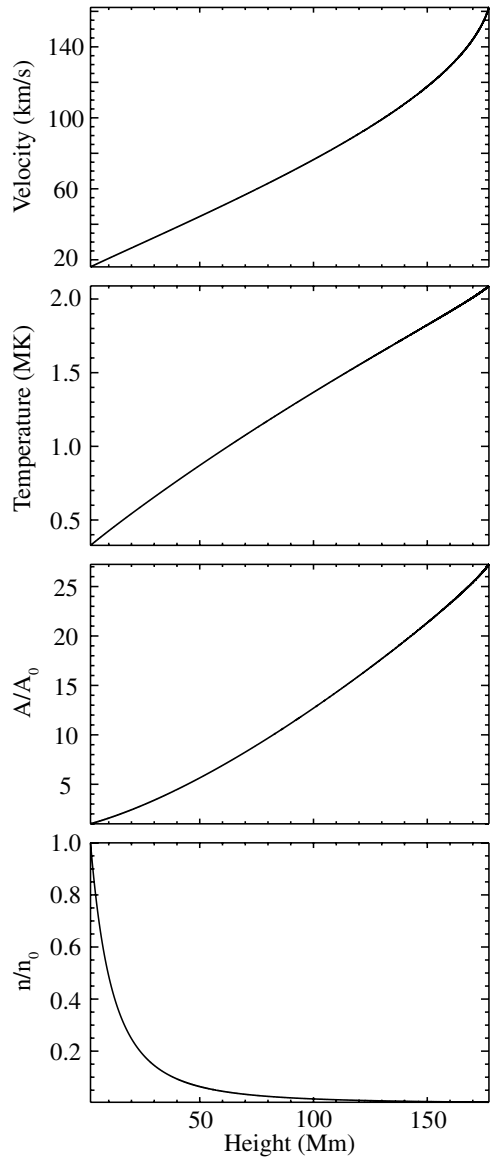

Figure 9. Height variation of plasma conditions in the case of $\nu = 3.6$ (Case II: empirical strong expansion model). The figure format is the same as Figure 8.

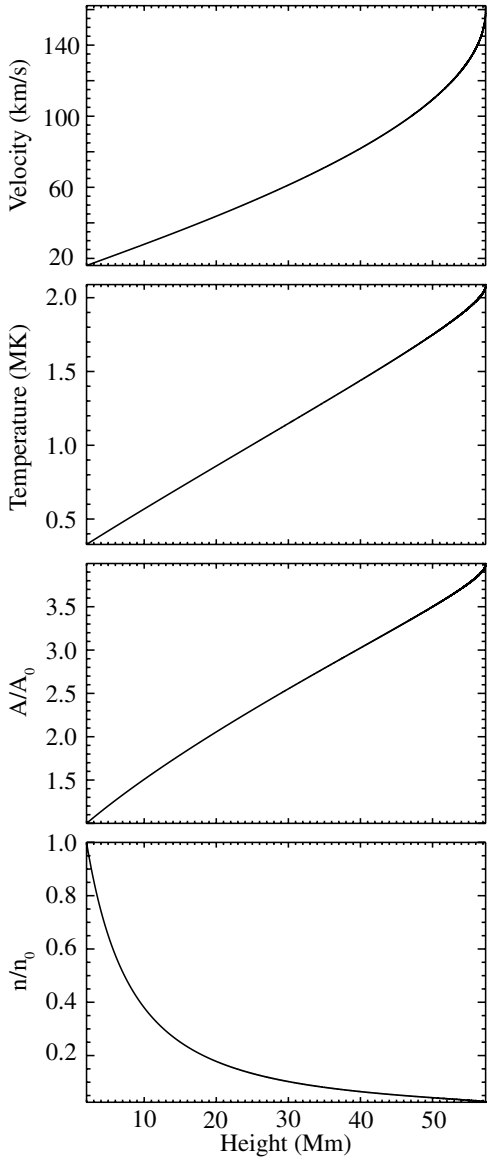

Figure 10. Height variation of plasma conditions in the case of $\nu = 1.5$ (Case III: empirical weak expansion model). The figure format is the same as Figure 8.

is the same as Figure 8. The upflow is linearly accelerated until a height of 150 Mm, and the velocity gradient becomes much steeper beyond 150 Mm. Roughly speaking, the temperature is increasing linearly in the entire region. The 2 MK plasma is located at 170 Mm. The cross-sectional area expands almost proportionally to the height from the solar surface, and it reaches around 25 at 150 Mm. Because the velocity and cross-sectional areas are almost proportional to the height, the density decreases with height ($\sim s^{-2}$). The density ratios at 100 and 170 Mm are $\sim$0.015 and 0.004, respectively. It is also remarkable that the temperatures at 100 and 170 Mm are $\sim$1.4 and 2 MK, respectively.

3.3.2. Weak Dependence on Temperature: Case III ($\nu = 1.5$)

The increase of cross-sectional area between 0.4 and 1.6 MK plasma should be around $\sim$1.6, which we already mentioned in Section 2. It seems that the cross-sectional area expands too much in the previous case (Case II). The above parameters are derived from the quiet-Sun observations. Therefore, those may be different when we discuss the cross-sectional area in the dimming region. Next, we assumed the parameters as $T_h = 10^6$ K, $\Gamma = 31$, and $\nu = 1.5$ for the relatively gradual expansion in the cross-sectional area (Case III). The results of height dependence in the dimming region are shown in Figure 10. The figure format is the same as Figure 8. The characteristics in Figure 10 are very similar to that in Figure 9. Roughly speaking, the velocity, temperature, and cross-sectional area are increasing linearly, and the density is decreasing with height ($\sim s^{-2}$). The difference between Figures 9 and 10 is the absolute value of the height from the solar surface. The maximum height is $\sim$60 Mm in Figure 10, but is 180 Mm in Figure 9. The temperatures at 40 and 55 Mm are 1.4 and 2 MK, respectively. The density ratios at 40 and 55 Mm are 0.063 and 0.03, respectively. Note that our result is not sensitive to T_h or Γ but sensitive to ν largely. We have tested our method with other parameters (not shown here).

One may think that the increase of the cross-sectional area between 0.4 and 1.6 MK plasma is still large when we assume $\nu = 1.5$. Assuming a much smaller value in ν ($\sim$1), the increase will become much smaller, and the height from the solar surface

becomes much lower. However, when we assume $\nu \sim 1$, there are double valued solutions in the higher temperature range. Thus we cannot obtain the realistic solution with $\nu \sim 1$.

3.4. Comparison between Cases I–III

Let us discuss which is the most realistic result within our three examples. One of the biggest differences between the three results is the height from the solar surface. In Case I, 1.4 MK plasma (Fe XII) is located around 7.5 Mm from the solar surface. On the other hand, 1.4 MK plasma is located around 100/40 Mm from the solar surface in Case II/III, respectively. Unfortunately, we do not have any observational information on the height in this event. However, some similar events that occurred in the limb showed that the line formation height of Fe XII (1.4 MK plasma) is $\lesssim$10 Mm. Balasubramaniam et al. (2010) discussed the flare event on 2006 December 6. The flare occurred in the same active region as our event (NOAA 10930), and their characteristics are also very similar to our event (e.g., eruptive flare, GOES class, CME associated flare). They also found the upflow at the boundary of the active region and the dark region (transient coronal hole) in Fe XII (see Figure 16 in Balasubramaniam et al. 2010). The upflow was observed only in the base of a flux tube ($\lesssim$10 Mm from the surface). These findings support our results in Case I. Furthermore, the increase of the cross-sectional area also supports Case I. The observation in Jin et al. (2009) indicates that the increases of the cross-sectional area between 0.4 and 1.6 MK plasma seem to be 1.6. Therefore, we conclude that the results in Case I are the most realistic.

4. TIME-DEPENDENT IONIZATION

We have discussed the height variation of the temperature-dependent upflow in the dimming region by using the steady hydrodynamic equation. To derive the relationship between the temperature and the velocity from the observations, we assumed an ionization equilibrium. Generally, fast flow and rapid heating may cause non-equilibrium ionization, and so far many papers have discussed the time-dependent ionization with models (e.g., Dupree et al. 1979; Reale & Orlando 2008; Ko et al. 2010; Imada et al. 2011) and observations (e.g., Kato et al. 1998; Imada et al. 2009; Murphy et al. 2011). It is plausible that the ionization equilibrium assumption is violated in our situation, because both the temperature and velocity rapidly increase with height. In this section, we try to evaluate the ionization equilibrium assumption in our results.

In order to study the effect of transient ionization, we have calculated the time evolution of ion charge states. In our EIS observations, most emission lines are from iron. Therefore, we concentrated on the time-dependent ionization of iron in this paper. The method we use to calculate the time-dependent ionization is the same as that described in Imada et al. (2011). The continuity equations for iron are expressed as follows:

$$\frac{\partial n_i^{\rm Fe}}{\partial t} + \nabla \cdot n_i^{\rm Fe}\mathbf{v} = n_e \left[n_{i+1}^{\rm Fe}\alpha_{i+1}^{\rm Fe} + n_{i-1}^{\rm Fe}S_{i-1}^{\rm Fe} - n_i^{\rm Fe}\left(\alpha_i^{\rm Fe} + S_i^{\rm Fe}\right)\right], \quad (13)$$

where $n_i^{\rm Fe}$ is the number density of the ith charge state of the iron, $\alpha_i^{\rm Fe}$ represents the collisional and dielectronic recombination coefficients, and $S_i^{\rm Fe}$ represents the collisional ionization coefficients. The ionization and recombination rates were calculated using Arnaud & Rothenflug (1985), Arnaud & Raymond (1992), and Mazzotta et al. (1998). Here we assumed that all ions and electrons have the same flow speed and temperature in the same position. The ionization and recombination coefficients (α and S) strongly depend on electron temperature and weakly depend on density. The timescale for ionization and recombination is proportional to n_e^{-1}.

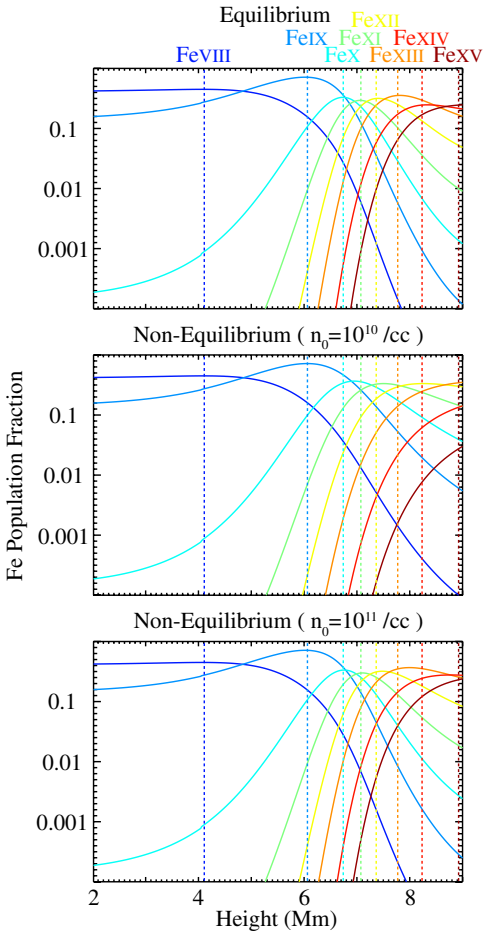

Figure 11. Time-dependent ionization in the case of $\mu = 45$ (Case I: super-radial expansion). From top to bottom, the results with ionization equilibrium, non-equilibrium ($n_0 = 10^{10}$ cm^{-3}), non-equilibrium ($n_0 = 10^{11}$ cm^{-3}) are shown, respectively. The vertical dotted lines show the heights of peak abundance in each element in the ionization equilibrium results (top).

(A color version of this figure is available in the online journal.)

To solve the time-dependent ionization, we need the absolute value of the density. We set the density at the base of the flux tube (n_0) to 10^{10} and 10^{11} cm^{-3}. These values are reasonable for the density in the upper chromosphere or lower transition region (e.g., Vernazza et al. 1981). Figure 11 shows the height variation of the iron charge states in the super-radial expansion model (Case I; Figure 8). From the top, the results of the ionization equilibrium calculation, time-dependent ionization calculation with the lower density assumption ($n_0 = 10^{10}$ cm^{-3}), and time-dependent ionization calculation with the higher density assumption ($n_0 = 10^{11}$ cm^{-3}) are shown. The peak abundances of each charge state with the ionization equilibrium assumption are shown with vertical dotted lines. From Fe VIII to Fe X, the ionization equilibrium assumption seems to be reasonable. On the other hand, it is clearly seen that the ionization equilibrium assumption is violated from Fe XI to Fe XV in the case of the lower density assumption. This is because there is a steep temperature and velocity gradient around 7 Mm. Even in the

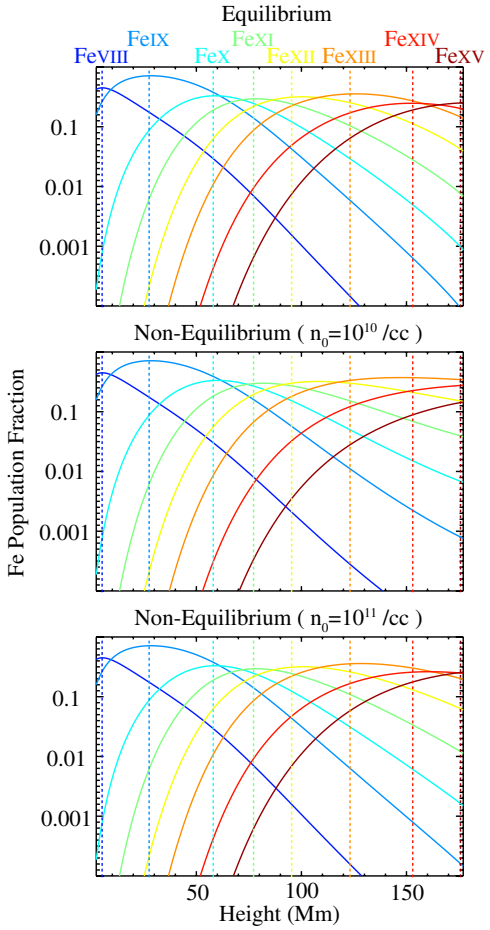

Figure 12. Time-dependent ionization in the case of $v = 3.6$ (Case II: empirical strong expansion model). The figure format is the same as Figure 11.
(A color version of this figure is available in the online journal.)

case of a higher density assumption, the ionization equilibrium assumption is violated in Fe XIV and Fe XV.

We also perform the same analysis in the empirical rapid expansion model (Case II; Figure 9). Figure 12 shows the height variation of the iron charge states in Case II. The figure format is the same as Figure 11. It is plausible that the ionization reaches the equilibrium stage in this mode, because the gradient of temperature and velocity in space is relatively gradual compared with the previous model. However, even in this case, the ionization equilibrium assumption is violated in Fe XIV and Fe XV. This is because the rapid expansion causes the low density in the high-temperature range, and the timescale of ionization increases. Therefore, in either case, the ionization equilibrium assumption may be violated in the higher temperature range.

The violation of the ionization equilibrium naturally causes the increasing of the line formation temperature. For example, the peak abundances of Fe XII in the case of the ionization equilibrium (top of Figure 11) are located around 7.5 Mm (the yellow dotted line). Thus, Fe XII represents ∼1.4 MK plasma, because the temperature at 7.5 Mm is 1.4 MK in Figure 8. However, the peak abundances of Fe XII in the case of time-dependent ionization (middle of Figure 11) are located around 8 Mm. This indicates that Fe XII represents ∼1.7 MK plasma, because the temperature at 8 Mm is 1.7 MK in Figure 8. In the higher temperature range, the line formation temperatures systematically increase by considering time-dependent ionization. Therefore, some modification to the relationship may be needed between

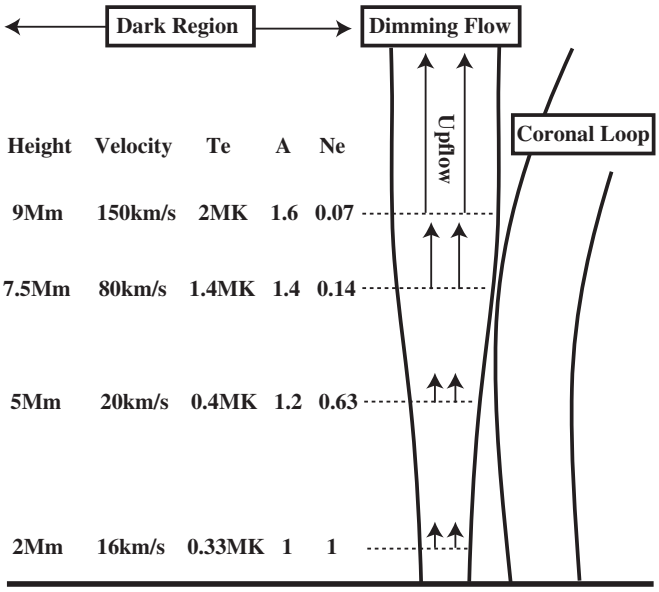

Figure 13. Schematic illustration of our observation and reconstruction in and around the dimming region. T_e shows the electron temperature in the dimming region. A and N_e show the cross-sectional area and electron density which are normalized at the base (2 Mm).

the velocity and temperature in Figure 5, especially in the higher temperature range. The relationship may become close to linear after considering the time-dependent ionization.

5. SUMMARY AND DISCUSSION

We have discussed the temperature-dependent upflow in the dimming region observed by *Hinode*/EIS. We have reanalyzed the dimming event on 2006 December 13 and described the previous results for this event. The observations show:

(1) the intensity in the dimming region dramatically drops within 30 minutes of the flare onset, and the dimming region reaches the equilibrium stage after ∼1, (2) the temperature-dependent upflows are observed in the dimming region during the equilibrium stage, and (3) the area of the dimming region also weakly depends on the temperature (the expansion factor is ∼1.6 between 0.4 and 1.6 MK plasma). We carried out the reconstruction of the temperature-dependent upflow by using our new method with the assumption that both the temperature and velocity depend on the height from the solar surface. The height variations of plasma conditions in the dimming region are demonstrated for three different cases, and we discussed which result is the most realistic. What we found from the reconstruction is as follows: (1) the super-radial expansion of the cross-sectional area is required to satisfy the mass conservation and momentum equations, (2) the temperature and velocity gradient with height become steep around 7 Mm from the solar surface, and (3) the ionization equilibrium assumption may be violated in the higher temperature range. What we found is summarized in Figure 13.

In our analysis, we assumed that both temperature and velocity depend on the height from the solar surface. We already mentioned that the other scenario (the multi-strand model) can also explain this observation. Note that it is still consistent even if we apply our result to the multi-strand model, because the higher temperature loop (∼2 MK) also contains the cold component (∼1 MK) at the base of the loop. The difference between the

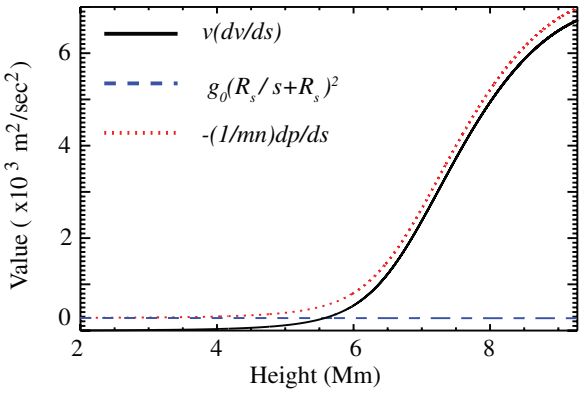

Figure 14. Each term in Equation (4) (Case I: super-radial expansion).
(A color version of this figure is available in the online journal.)

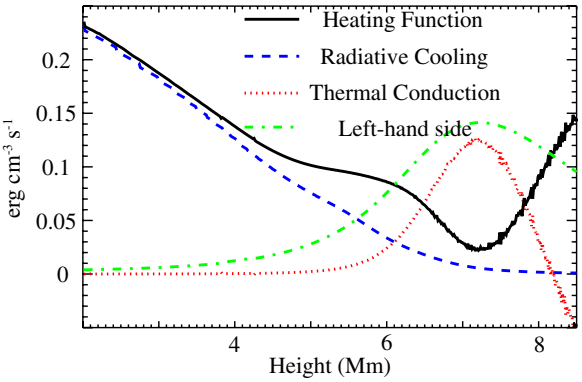

Figure 15. Energy balance in the dimming region (Case I: super-radial expansion).
(A color version of this figure is available in the online journal.)

two scenarios is that the heating and acceleration are stopped before reaching 2 MK in some loops.

Let us discuss the impact of the temperature gradient to the flow acceleration. To understand intuitively, we assume $p \propto e^{-s}$ and $T = \lambda_1 s + \lambda_2$, where $\lambda_{1,2}$ is the positive parameter. After substituting $p \propto e^{-s}$ and T to Equation (3), we can derive $n \propto (\lambda_1 s + \lambda_2)^{-1} e^{-s}$. Then we found that the first term in right-hand side in Equation (4) ($(-1/mn)dp/ds$) is proportional to $\lambda_1 s + \lambda_2$. Roughly speaking, the second term in the right-hand side of Equation (4) is negligible. Therefore, the steep temperature gradient causes the rapid acceleration. The steep temperature gradient causes the steep density drop. This is the reason why the strong temperature gradient causes the strong acceleration. Figure 14 shows each term in Equation (4) in Case I, and we can find that the trend of $(-1/mn)dp/ds$ is very similar to that of the temperature in Figure 8.

We also perform the time-dependent ionization calculation in our models and found that the ionization equilibrium assumption may be violated in the higher temperature range. This naturally causes the increasing of the line formation temperature, and we need some modification to the relationship between the velocity and temperature in Figure 5. Furthermore, the modification causes another modification in our reconstruction of the dimming region. It may be possible to find a reconstruction solution that can satisfy both the hydrodynamic equation and the time-dependent ionization. However, the time-dependent ionization process heavily depends on the absolute value of the density. Unfortunately, we do not have any pairs of emission lines for density diagnostics in our observation. Thus we cannot conclude whether the modification is really needed or not at this stage.

We now discuss the energy balance in our model. The energy equation in quasi-steady flow can be written as follows:

$$\frac{3}{2} v p \frac{1}{T}\frac{dT}{ds} + p\frac{dv}{ds} + v p \frac{1}{A}\frac{dA}{ds} = \frac{1}{A}\frac{d}{ds}\left(\kappa_0 A T^{\frac{5}{2}}\frac{dT}{ds}\right) - n^2\Lambda(T) + H, \quad (14)$$

where κ_0, $\Lambda(T)$, and H are the thermal conductivity along the magnetic field line, the radiative loss function, and the heating function. From our reconstruction of the flow in the dimming region, we can derive most of the terms in Equation (14). The exceptions are the absolute value of the density and the heating function. Thus we can estimate the heating function with the assumption of density at the base of the flux tube. We have calculated the heating function with $n_0 = 2.5 \times 10^{10}$ cm^{-3} in Case I. Figure 15 shows the energy balance in the dimming region. The solid (black), dashed (blue), dotted (red), and dot-dashed (green) lines show the height variation of the heating function, radiative cooling, thermal conduction, and left-hand side of Equation (14), respectively. At the bottom of the flux tube, the radiative cooling is dominated because of the low-temperature and high-density plasma. Therefore, the heating function should be large enough to maintain energy balance. There is a steep gradient in the velocity and temperature between 6 and 7 Mm in Figure 8. Thus the enthalpy transport and thermal conduction are dominated in this region. Above 7 Mm, the temperature gradient becomes gradual. This naturally causes the rapid reduction of the thermal conduction, although the enthalpy transport reduces gradually. Thus an increase in the heating function is required. Our result in Case I suggests that the strong heating function may be located above 7 Mm. Note that most of Equation (14) is dependent on the absolute value of the density, and the dependence on the density is different in the each term; radiative cooling $\propto n^2$, left-hand side $\propto n^1$, and thermal conduction $\propto n^0$. Unfortunately, we do not have the observational information of the density. Thus, we do not discuss the absolute value of the heating function at this stage.

Density diagnostics are crucial for the modeling of the dimming region. Consistent modeling, taking care of the time-dependent ionization and energy equation of the dimming region with the density diagnostics is for future work. Another important question is the stability of the dimming flow in the category of hydro and/or magnetohydrodynamics. So far, the stability of coronal loops in many kinds of instabilities was tested (e.g., Parker 1953; Hood & Priest 1980; Zweibel 1981). The dimming flow seems to persist for a long period. The steady solutions dramatically change in some cases when the conditions are slightly modified. Furthermore, the critical point seems very close to the solar surface, although it is not clear whether the flow passes through a critical point or not. It is physically important whether the flows become super sonic or not. This may also affect the stability of the dimming region. The stability analysis of the dimming region is also a topic for future work.

Hinode is a Japanese mission developed and launched by ISAS/JAXA, collaborating with NAOJ as a domestic partner, NASA and STFC (UK) as international partners. Scientific operation of the *Hinode* mission is conducted by the *Hinode* science team organized at ISAS/JAXA. This team mainly consists of scientists from institutes in the partner countries.

Support for the post-launch operation is provided by JAXA and NAOJ (Japan), STFC (U.K.), NASA (U.S.A.), ESA, and NSC (Norway).

This work was partially supported by the Grant-in-Aid for Young Scientists Start-up (21840062), by the Grant-in-Aid for Scientific Research B (23340045), by the JSPS Core-to-Core Program (22001), by the JSPS fund R53 ("Institutional Program for Young Researcher Overseas Visits," FY2009-2011) allocated to NAOJ, and by the NINS Inter-institute collaborative program for Creation of New Research Area (Head Investigator: T. Watanabe). We also acknowledge partial support by the Center for Magnetic Self Organization (NSF PHY0821899) and the hospitality of the University of Wisconsin.

REFERENCES

Arnaud, M., & Raymond, J. 1992, ApJ, 398, 394
Arnaud, M., & Rothenflug, R. 1985, A&AS, 60, 425
Asai, A., Hara, H., Watanabe, T., et al. 2008, ApJ, 685, 622
Attrill, G., Harra, L. K., van Driel-Gesztelyi, L., et al. 2010, Sol. Phys., 264, 119
Attrill, G., Nakwacki, M. S., Harra, L. K., et al. 2006, Sol. Phys., 238, 117
Balasubramaniam, K. S., Cliver, E. W., Pevtsov, A., et al. 2010, ApJ, 723, 587
Carmichael, H. 1964, in NASA Special Publication 50, The Physics of Solar Flares, ed. W. N. Hess (Washington, DC: NASA), 451
Chae, J., Yun, H. S., & Poland, A. I. 1998, ApJS, 114, 151
Craig, I. J. D., & McClymont, A. N. 1986, ApJ, 307, 367
Culhane, J. L., Harra, L. K., James, A. M., et al. 2007, Sol. Phys., 243, 19
Delaboundiniére, D. A., Artzner, G. E., Brunaud, J., et al. 1995, Sol. Phys., 162, 291
Dolla, L. R., & Zhukov, A. N. 2011, ApJ, 730, 113
Dowdy, J. F., Emslie, G. A., & Moore, R. L. 1987, Sol. Phys., 112, 255
Dupree, A. K., Moore, R. T., & Shapiro, P. R. 1979, ApJ, 323, L101
Gabriel, A. H. 1976, Phil. Trans. R. Soc. A, 281, 339
Harra, L. K., Hara, H., Imada, S., et al. 2007, PASJ, 59, S801
Harra, L. K., Mandrini, C. H., Dasso, S., et al. 2011, Sol. Phys., 268, 213
Hirayama, T. 1974, Sol. Phys., 34, 323
Hood, A. W., & Priest, E. R. 1980, Sol. Phys., 66, 113
Imada, S., Hara, H., & Watanabe, T. 2009, ApJ, 705, L208
Imada, S., Hara, H., Watanabe, T., et al. 2007, PASJ, 59, S793
Imada, S., Hara, H., Watanabe, T., et al. 2008, ApJ, 679, L155
Imada, S., et al. 2011, ApJ, in press
Jin, M., Ding, M. D., Chen, P. F., Fang, C., & Imada, S. 2009, ApJ, 702, 27
Kahler, S. W. 1992, ARA&A, 30, 113
Kato, T., Fujiwara, T., & Hanaoka, Y. 1998, ApJ, 492, 822
Ko, Y. -K., Raymond, J. C., Vršnak, B., & Vujić, E. 2010, ApJ, 722, 625
Kopp, R. A., & Pneuman, G. W. 1976, Sol. Phys., 50, 85
Kosugi, T., Matsuzaki, K., Sakao, T., et al. 2007, Sol. Phys., 243, 3
Kubo, M., Yokoyama, T., Katsukawa, Y., et al. 2007, PASJ, 59, S779
Landi, E., Del Zanna, G., Young, P. R., et al. 2006, ApJS, 162, 261
Mazzotta, P., Mazzitelli, G., Colafrancesco, S., & Vittorio, N. 1998, A&AS, 133, 403
Minoshima, T., Imada, S., Morimoto, T., et al. 2009, ApJ, 697, 843
Murphy, N. A., Raymond, J. C., & Korreck, K. E. 2011, ApJ, 735, 17
Ohyama, M., & Shibata, K. 1998, ApJ, 499, 934
Orlando, S., Peres, G., & Serio, S. 1995, A&A, 294, 861
Parker, E. N. 1953, ApJ, 117, 431
Parker, E. N. 1958, ApJ, 128, 664
Rabin, D. 1991, ApJ, 383, 407
Reale, F., & Orlando, S. 2008, ApJ, 684, 715
Robbrecht, E., & Wang, Y.-M. 2010, ApJ, 720, L88
Rust, D. M. 1983, Space Sci. Rev., 34, 21
Sterling, A. C., & Hudson, H. S. 1997, ApJ, 491, L55
Sturrock, P. A. 1966, Nature, 211, 695
Teriaca, L., Falchi, A., Cauzzi, G., et al. 2003, ApJ, 588, 596
Thompson, B. J., Plunkett, S. P., Gurman, J., et al. 1998, Geophys. Res. Lett., 25, 2461
Tsuneta, S., Hara, H., Shimizu, T., et al. 1992, PASJ, 44, 63
Ugarte-Urra, I., & Warren, H. P. 2011, ApJ, 730, 37
Vernazza, J. E., Avrett, E. H., & Loeser, R. 1981, ApJS, 45, 635
Warren, H. P., Ugarte-Urra, I., Young, P. R., & Stenborg, G. 2011, ApJ, 727, 58
Yashiro, S., Akiyama, S., Gopalswamy, N., & Howard, R. 2006, ApJ, 650, 143
Yokoyama, T., Akita, K., Morimoto, T., Inoue, K., & Newmark, J. 2001, ApJ, 546, L69
Young, P., Del Zanna, G., Mason, H. E., et al. 2007, PASJ, 59, S857
Zweibel, E. G. 1981, ApJ, 249, 731